Bulletin of the
Seismological Society of America

Vol. 64 June 1974 No. 3

PARKFIELD, CALIFORNIA, EARTHQUAKE OF JUNE 27, 1966: A THREE-DIMENSIONAL MOVING DISLOCATION

By M. D. Trifunac and F. E. Udwadia

ABSTRACT

Recordings from five strong-motion accelerograph stations have been used to derive a three-dimensional dislocation model for the Parkfield Earthquake. The model consists of a buried fault which extends from a depth of 3 km to a depth of 9 km below the ground surface. It appears from the analysis, which considers various fault lengths, that the zone of significant faulting was the 20-km-long northwestern section of the fault. The rupture velocity has been found to be between 2.4 and 2.5 km/sec and the dislocation amplitudes have been found to be about 120 cm. There have been comparisons made of the model results with geodetic data on static deformations and creep measurements following the event. In contrast with several other source mechanism studies of the Parkfield event, this model yields a picture which appears to be very consistent with both the dynamic strong-motion measurements as well as the available geodetic and creep data.

Introduction

This paper represents the continuation of our efforts at gaining a deeper understanding of the details of energy release during earthquakes. By using the elementary form of the dynamic dislocation theory (Haskell, 1969), a suitable three-dimensional dislocation model has been worked out for the Parkfield event. As demonstrated earlier (Trifunac, 1974), such a model can explain the gross long-period features of the measured near-field strong ground motions. Although the search for a suitable model involves a nonunique inverse approach, the choice of the "best" dislocation model can be substantially guided by independent inferences based on static and dynamic computations.

The Parkfield Earthquake is a well-documented event. The main shock and several aftershocks were recorded at five strong-motion stations of the Cholame-Shandon array (Cloud and Perez, 1967) in addition to other teleseismic data. Even though the strong-motion stations were located only on one side of the fault, the excellent quality accelerograms obtained can be used for source mechanism studies (Trifunac *et al.* 1973).

The purpose of this paper is two-fold. First, through a study of the dynamic faulting process, we will analyze the mechanism of energy release, thereby clarifying and resolving some of the contradictory interpretations of the event (e.g., Scholz *et al.*, 1969 and Aki, 1968). Second, the inversion technique, so far tested only on the San Fernando, California, earthquake, which was a thrust fault, will be applied to a strike-slip fault along the San Andreas. The applicability of such a simple inversion scheme will be tested through comparisons with available information from geodetic and creep data.

Summary of Field Observations, Aftershock Studies and Previous Source Mechanism Work

The earthquake occurred on June 27, 1966 at 9:26 p.m. Pacific daylight time (04:26:13.4 GMT, June 28, 1966) beginning with two light foreshocks (magnitudes 2–3) at

6:00 p.m. and 6:15 p.m. on June 27 (McEvilly, 1966), being followed by a stronger foreshock of magnitude 5.1 at 9:09 p.m. Magnitude estimates of the main shock range from 5.3 to 6.5 [m_b = 5.3 (USGS), M_L = 5.5 (Berkeley), M_L = 5.8 (Pasadena), M_S = 6.5 (Palisades)], and numerous aftershocks continued for many weeks (Eaton *et al.*, 1970).

Since the earthquake occurred at night, nothing is known about the surface faulting which immediately followed the main shock. The first observations that were made about 10 hr after the main shock (Allen and Smith, 1966) indicated that the white line on Highway 46 (Figure 1) had been offset by 4.5 cm in a right-lateral sense. The extrapolation of the displacement curve back to the origin time indicates that there was essentially zero offset at the time of the main shock (Wallace and Roth, 1967; Figure 25).

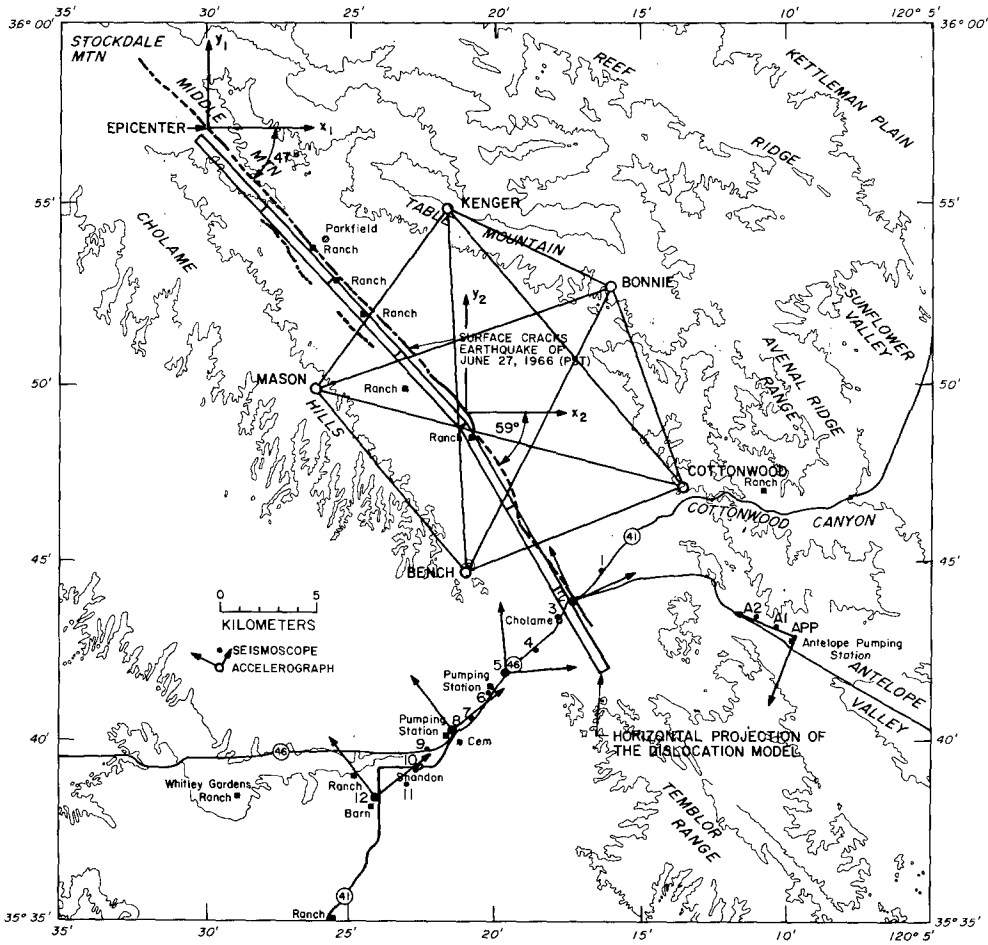

FIG. 1. Map showing the epicenter of the Parkfield Earthquake, the fault zone, the horizontal projection of the dynamic dislocation model, locations of accelerographs and seismoscopes and the geodetic pentagón.

An indication of the rupture length may be obtained from the narrow band (about 5 m wide) of *en echelon* cracks that were exposed on the surface of the alluvium. If some isolated cracking north of the epicenter were to be neglected, then, on the basis of these surface cracks, the rupture length may be estimated to be about 33 km. The overall dense distribution of aftershocks, however, suggests a source length of 27 km (McEvilly *et al.*, 1967), whereas the location of 13 aftershocks which immediately followed the earthquake and which were recorded by the strong-motion accelerograph array indicates

only a 20-km length of rupture (Murray, 1967). The southernmost group of these early aftershocks consisted of seven events and was centered near the origin of the x_2, y_2 coordinate system shown in Figure 1. A detailed analysis of the aftershocks which occurred between the 3rd and the 82nd day following the main shock has been carried out by Eaton *et al.* (1970). They fitted a reference plane to 474 well-located aftershocks (with a standard deviation of 0.45 km from the plane) and found the strike and dip to be N39°W and 86°SW, respectively. The foci of 95 per cent of these aftershocks were located at depths ranging from 1 to 12 km, with no aftershocks occurring deeper than 15 km and with a high concentration of foci at depths between 2 and 4 km and also between 8 to 10 km. A pronounced minimum of aftershock activity at depths between 5 and 7 km was observed. A large majority of the aftershocks studied by Eaton *et al.* (1970) showed right-lateral strike-slip displacement on surfaces which were nearly parallel to the reference plane striking N39°W and dipping 86°SW.

Based upon the *P*-wave onset direction data for the main shock, McEvilly (1967) found the allowable strike and dip angles to range from a strike of N35°W and a dip of 88°NE to a strike of N24°W and a dip of 85°SW. The strike of the observed surface cracking was about N40°W for the northern section and about N35°W for the southern section of the fault (Figure 1). The coordinates of the origin of the main shock were found to be 35°57.3′N and 120°29.9′W.

Accelerographs at Cholame approximately 30 km down the fault trace from the epicenter have recorded several aftershocks which had occurred during the first 3 min following the main shock (Murray, 1967). The $S-P$ times for these events decreased from about 5 sec or more for the main shock to about 2 sec or less for the aftershocks which occurred about 2 min later, suggesting that the fault propagated southeastward for a distance of about 20 km from the epicenter (McEvilly *et al.*, 1967).

Eaton (1967) estimated the rupture velocity to be 2.2 km/sec by using the motion of a radio time recorder operated near the origin of the coordinate system x_2, y_2 in Figure 1. Zeroes of the Love- and Rayleigh-wave spectra are consistent with this rupture velocity (Filson and McEvilly, 1967; Aki, 1968). Assuming that the strong horizontal acceleration pulse recorded at station 2 (Figure 1), 30.5 km southeast of the epicenter, was caused by the rupture propagating past the accelerograph, Filson and McEvilly (1967) obtained an average rupture velocity of 2.3 ± 0.1 km/sec. All of the above findings seem to indicate that the main shock originated near the instrumentally determined epicenter and propagated southeastward for at least about 20 km and at most about 35 km.

Brown and Vedder (1966) explored the surface fracture zones from June 29 to July 15, 1966. Two well-defined fracture zones were found: the main zone could be continuously traced for about 37 km, whereas the discontinuous subsidiary zone, which extended for about 9 km, lay parallel to, and about 1 km, southwest of the main fault zone (Figure 1).

A summary of the geological characteristics of the crustal blocks NE and SW from the San Andreas Fault has been presented by Eaton *et al.* (1970). Several short but detailed refraction profiles in the Parkfield-Cholame region were also conducted to determine the structure in the upper crust. Figure 2, redrawn from Eaton *et al.* (1970), shows simple NE and SW models composed of horizontal layers of constant velocity. We added to this figure a plot of the rigidity μ in dyne/cm^2 versus depth. The approximate value of μ was estimated by using the empirical formula of Birch (1961), $\rho = 0.77 + 0.302\alpha$, which gives the density ρ in terms of the *P*-wave velocity α.

Wallace and Roth (1967) and Smith and Wyss (1968), reporting on the observations of fault creep which followed the earthquake, found that the creep decayed off after the main shock in a logarithmic manner similar to the fall-off of aftershock activity. They showed that immediately after the earthquake the relative displacements on the two sides of the

fault were either nil or very small and that about 1 year after the earthquake the average displacement over the 30-km distance approached a value of about 25 cm.

The Department of Water Resources of California established a geodetic pentagon across this portion of the San Andreas Fault in October, 1965. Following the Parkfield earthquake both the Department of Water Resources (Department of Water Resources, 1968a, b; Morrison *et al.*, 1966) and the U.S. Coast and Geodetic Survey (Meade, 1967) remeasured their geodimeter and triangulation networks. Repeated measurements on the pentagon, which were carried out during the 2 weeks following the earthquake, indicate that relative to the measurements made before the earthquake, the stations, which were 6 to 8 km from the fault, had moved about 20 cm in the right lateral sense.

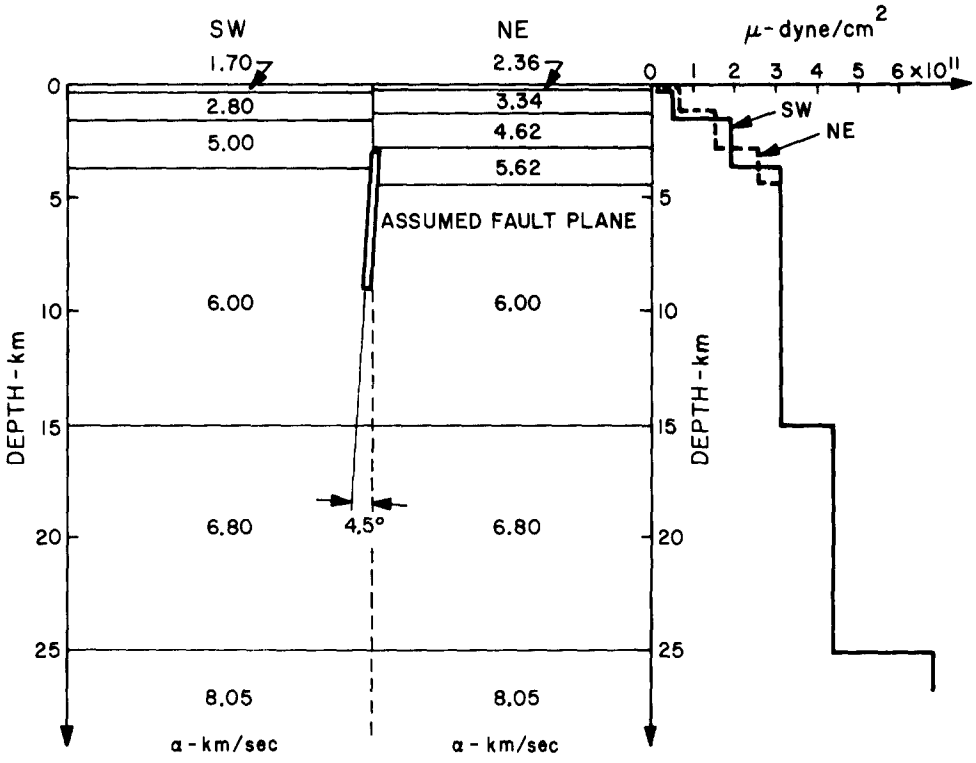

FIG. 2. Dual crustal model along the San Andreas Fault in the Parkfield-Cholame region (Eaton *et al.*, 1970).

The strong ground motion was recorded by an array of five strong-motion accelerograph stations (Stations 2, 5, 8, 12 and Antelope Pumping Station called Temblor; Figure 1) and 15 seismoscopes across the San Andreas Fault at Cholame (Cloud and Perez, 1967; Hudson and Cloud, 1967). Although a ground acceleration of about 50 per cent of gravity was recorded at the fault, the short impulsive ground motion caused little damage to structures due to its short duration (Housner and Trifunac, 1967).

Aki (1968) was the first in interpreting the mechanism of the main shock by synthesizing the strong ground motion recorded at Station 2 (Figure 1). He found the fault dislocation to be about 60 cm from a depth of 3 km to less than 100 meters from surface and concluded that the recorded strong ground motion at Station 2 was essentially dominated by the fault motion in the close proximity of the recording station. Since the overall surface

fault offset in the vicinity of Station 2 was at most several centimeters (Allen and Smith, 1966), Aki hypothesized "a process in which the propagation of dislocation to the surface is prevented at a certain shallow depth," in order to reconcile his dynamic model which had a dislocation amplitude of 60 cm. Aki notes in his discussion that the Fukui earthquake of 1948 (Kasahara, 1964) was a similar example in which no clear surface fault offset was observed except for a narrow zone about 30 km long which contained numerous small fissures. Geodetic measurements, however, showed a deformation pattern which could be explained quantitatively by a buried fault covered by 3-km thick sediments.

The buried fault model for the Parkfield earthquake was further investigated by Scholz *et al.* (1969), who postulated a fault model 40 km long extending from a depth of 4 km to a depth of 10 km and having a dislocation amplitude of 30 cm. Although their model agrees favorably with the distribution of aftershocks (Eaton *et al.*, 1970) and creep following the earthquake (Wallace and Roth, 1967; Smith and Wyss, 1968), it underestimates the geodetic displacements by a factor of about 2 (Morrison *et al.*, 1966).

Using an approach different from that of Aki (1968), Haskell (1969) calculated the synthetic ground motion for the N65E component of ground shaking at Station 2 (Figure 1). With a fault length of 19.8 km, a fault width of 2.48 km, and a dislocation velocity equal to 2.2 km/sec, he found the dislocation amplitude to be 93 cm, an order of magnitude greater than the offset observed along the surface fault trace (Allen and Smith, 1966). He therefore concluded that the offsets observed along the surface fault trace were not necessarily representative of the fault dislocation at depth. Anderson (1973) presented a moving dislocation model with a dislocation amplitude of 25 cm and a dislocation velocity between 2.8 and 3.0 km/sec, while Tsai and Patton (1973) selected a different model with a propagation velocity of 2.2 km/sec and a dislocation amplitude of 200 cm.

In this paper, we attempt to resolve some of the controversial results summarized above by fitting a moving dislocation model to strong-motion data obtained from five stations (Trifunac *et al.*, 1973b) and the post-earthquake static field measured by the geodetic pentagon across the San Andreas Fault (Morrison *et al.*, 1966).

A Simple Dislocation Model

We use the Haskell (1969) formulation for waves radiated by a plane dislocation in an infinite elastic medium which yields the ground motion at a point (X_1, X_2, X_3) for a fault in the X_1–X_2 plane. A model of this type consisting of a rectangular fault of length L and width H is illustrated in Figure 3. The fault lies in a plane striking Eθ°S and dipping ψ°Nθ E. The direction X_1 of the progressing plane dislocation front, travelling at the velocity v, is given by φ, while the final direction of the dislocation vector depends on the amplitudes D_1 and D_2.

Computation of the three ground-motion components at equal time intervals requires numerical integration over that section of the fault plane for which the dislocation at the corresponding time is nonzero. Since the integration technique used in this paper is identical to that used in our previous work (Trifunac, 1974), no details will be repeated.

It is important to note that the Haskell representation (1969) gives the exact solution for a homogeneous infinite medium only. It incorporates the static terms as well as the dynamic near-field $(1/r^4)$, intermediate $(1/r^2)$, and the far-field $(1/r)$ terms, where r is the distance between the fault and the observation point. It does not include the surface waves which undoubtedly become important in the later portion of the strong ground motion. For this reason Haskell's (1969) representation can be used only to model approximately the recorded near-field motions and the body-wave motions. Although it may appear that the infinite space model may be too crude and the surface waves cannot be neglected,

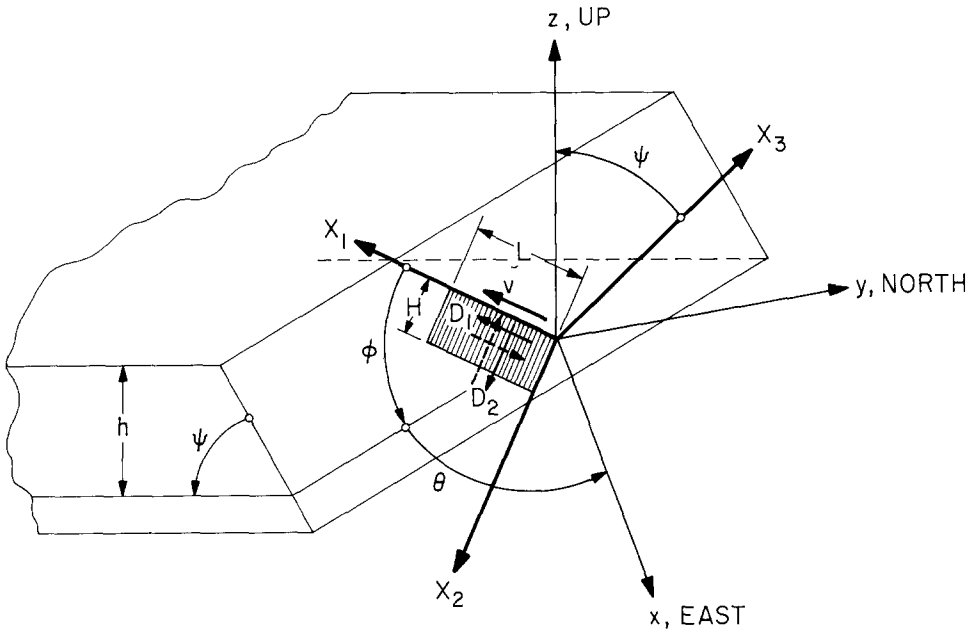

FIG. 3. Geometrical setting of an elementary fault model.

our study of the San Fernando earthquake (Trifunac, 1974) shows that a plausible three-dimensional model, which favorably agrees with other independent inferences of the source mechanism, may be obtained in spite of these and other simplifying assumptions. The stress-free boundary conditions at the half-space surface can be approximately satisfied by the infinite space model in the case of a vertical fault surface with strike-slip faulting. The single fault model in the infinite space, used in this study, with doubled amplitudes to account for the free surface effect also violates the stress-free surface boundary conditions. Nevertheless, we expect that when this approximate theory is applied to the modeling of the Parkfield earthquake, it should yield more valuable results than those obtained for the San Fernando thrusting fault model (Trifunac, 1974), since strike-slip faulting on a vertical fault plane should be more suitable for applying Haskell's (1969) infinite space theory.

STRONG-MOTION ACCELEROGRAPH DATA

The strong-motion array, which consisted of five AR-240 accelerographs and 15 seismoscopes, had been installed only shortly before the earthquake as a cooperative venture of the California Department of Water Resources and the U.S. Coast and Geodetic Survey (Cloud and Perez, 1967; Housner and Trifunac, 1967). The array is nearly perpendicular to the trend of the San Andreas Fault in the Cholame Valley and lies along Highway 46 which runs through Cholame and Shandon. There are 12 seismoscopes and four accelerograph stations (Stations 2, 5, 8 and 12) along this line. Another group consisting of three seismoscopes and one accelerograph (Temblor Station) is located near the Antelope Pumping Station about 10 km east of Shandon. These are all shown in Figure 1. With the exception of the component parallel to the fault at Station 2, all instruments performed very well during the earthquake and excellent acceleration records were obtained from the main shock as well as from several foreshocks and aftershocks (Murray, 1966). The original accelerograph recordings (Cloud and Perez,

1967), computed ground velocity, displacement and response spectra (Housner and Trifunac, 1967), the seismoscope recordings (Hudson and Cloud, 1967) and the damage caused by the earthquake (Cloud, 1967) are all described in the literature.

It is best to have strong-motion stations close to and surrounding the fault for the source mechanism studies. Proximity of the stations minimizes the unknown travel path effects, and to have stations surrounding the fault increases the accuracy of the inferred fault geometry, the slip vector and the direction of the spreading dislocation. For the Parkfield earthquake, however, only the five accelerograms from the Cholame–Shandon array are available. As shown in Figure 1, these stations are located at the southeastern end of the fault plane about 30 to 40 km southeast from the epicenter. This may cause the parameters of the source mechanism derived from these stations to be affected in a systematic way by the geological formations between the fault and the stations.

The instrument types, the natural frequencies of all transducers, and the corresponding fractions of critical damping are all given in Table 1. This table also lists the assumed *S*-wave arrivals measured from the triggering time for each instrument. Computed ground

TABLE 1
INSTRUMENT TYPES AND CHARACTERISTICS

Station	*S*-time (sec)	Component	T_n (sec)	Damping % Critical	Instrument Type
Cholame-Shandon, no. 2	1.8	N 65°E	0.064	57.4	
		N 25°W*	—	—	AR-240
		Down	0.056	54.0	
Cholame-Shandon, no. 5	4.2	N 05°W	0.051	37.0	
		N 85°E	0.053	59.9	AR-240
		Down	0.054	51.2	
Cholame-Shandon, no. 8	1.4	N 50°E	0.051	59.9	
		N 40°W	0.051	55.2	AR-240
		Down	0.052	59.9	
Cholame-Shandon, no. 12	2.0	N 50°E	0.058	59.2	
		N 40°W	0.056	56.3	AR-240
		Down	0.057	57.4	
Temblor	1.0	N 65°W	0.060	52.8	
		S 25°W	0.058	57.4	AR-240
		Down	0.060	58.3	

* This component malfunctioned and left no recorded trace during the Parkfield sequence.

displacement curves used in the subsequent analysis were taken from the Volume II, Part B, *Report No. EERL 72-50* (Trifunac *et al.*, 1973b) which contains the corrected accelerograms and integrated velocity and displacement curves. These data are band-pass filtered from 0.07 to 25 Hz (Trifunac, 1971; 1972).

FINDING THE "BEST" DISLOCATION MODEL

The process of selecting the best dislocation model from the models that have been selected by the trial and error procedure is described in detail in our previous paper

(Trifunac, 1974). Here we explain only the main principles of this selection. First, using Haskell's (1969) representation, the displacement versus time is calculated for the selected number of stations used in this analysis. The calculation is carried out independently for every rectangular fault element assuming that the dislocation $D_1 = 1$, and for the specified dislocation velocity v and the dislocation rise time T. In this way, if there are K fault elements, we obtain K displacement time histories for every component of ground motion. We assume that in the Parkfield earthquake the faulting has been of the pure strike-slip type so that $D_2 = 0$ (Figure 3; Trifunac, 1974). Having calculated $3KJ$ displacement histories (where J is the total number of stations, each having 3 components of recorded ground motion and using a least-squares-fitting technique) we find the "best" K dislocation amplitudes which now represent the dislocation model sought.

We note that although the above scheme presents us with a way of finding the best set of dislocation amplitudes, it does not represent a complete inverse problem approach, since many other parameters have to be guessed. The fault shape, the dislocation velocity, and the rise time all have to be assumed before the contributions from each fault element can be calculated. Furthermore, Haskell's (1969) formulation assumes an infinite, elastic, and homogeneous space. Since earthquakes are recorded in the inhomogeneous inelastic half-space, using the simple model, we can expect to solve only for the gross features of the dislocation process in the frequency band that is not seriously affected by the geology and the transmission path. Since the infinite space model eliminates all surface waves, the present approach might be seriously affected by the surface-wave contributions present in the recorded ground motion. Using the near-field records of strong ground motion at distances where the surface waves have not been established yet, one can significantly reduce this difficulty. This is another illustration of the usefulness of recording close-in ground motions.

In adopting the infinite space homogeneous model we are, of course, eliminating not only the surface waves from the real earth problem but also the scattering and diffraction and thus the resulting attenuation with distance that is caused by the geological inhomogeneities and surface topography. Since, in general, these effects become significant when the wavelength of seismic waves becomes comparable to the "size" of geological discontinuities, the simplifying assumption of homogeneity forces us to restrict our attention to a frequency band that does not contain short wavelengths. Since the recorded ground displacements emphasize the long-period contents of strong ground motions, we therefore prefer to use ground displacements rather than ground velocity in the least-squares-fitting procedure.

Closely connected with this is the problem of the unknown dislocation function. Since we know virtually nothing about the typical time and space dependence of real earthquake dislocations, we have to assume simple functions characterized with the least number of parameters. As in the case of the homogeneity assumption, we have to concentrate on the gross parameters affecting the long-wave amplitudes (final dislocation amplitudes D_i and the rise time T), since the number of available strong-motion recordings, interspacing of instruments, and their distance from the fault once again limit the frequency band which we can use in deciphering the details of the dislocation function. From this viewpoint one might think of Haskell's (1969) ramp function as being an approximation to the "low-pass filtered" actual dislocation function.

Restrictions on the accuracy and the usable band width of the recorded ground motion are imposed by the transducer type and the digitization and processing noise (Trifunac *et al.*, 1973a). The high-frequency limit of the recorded accelerograms equals 25 Hz and therefore does not pose any restrictions in this analysis, since we are not dealing with frequencies higher than 1 Hz. On the other hand, the low-frequency limit of the usable

frequency band equals about 0.07 Hz and does lead to serious restrictions since the D.C. contributions to the near-field ground motion cannot be used in the search of the theoretical model. Another difficulty in using the presently available type of strong-motion accelerographs in this source mechanism work is that each instrument is triggered independently so that the absolute or common times of all recorded signals are not available. This makes it difficult to find the relative position in time of various accelerograms—one has to assume that the identification of some characteristic wave propagating with a known velocity may be used for this purpose. Although some errors are always inevitable, it has been thus far possible to successfully identify the *S*-wave arrivals on most of the strong-motion accelerograms. These arrival times, measured from the instrument triggering time, are listed in Table 1 for all accelerograms used in this paper.

The epicenter for the theoretical model has been chosen to coincide with the instrumentally determined epicenter [35°57.3′ (N), 120°29.9′ (W)] (Figure 1), whereas the geometry of the fault plane has been selected on the basis of the aftershock data of Eaton *et al.* (1970). The histograms of the number of aftershocks plotted versus depth using these data indicated two depths of high aftershock activity equal to 2.5 and 9.5 km for the northwestern section of the fault and 3.5 and 8 km for the southeastern section. In this paper, we assume that the high rate of aftershock occurrence delineates the ends of the dislocation surface and that these depths are close to 3 and 9 km for the whole fault plane. This interpretation of aftershock data is, of course, based on the assumption that the high stress concentration near the edge of a dislocation is the key factor leading to a higher aftershock activity there.

Eaton *et al.* (1970) found that the strike of a single plane fitted to the well-located hypocenters is N39°E and that it dips 85° toward the southwest. The pattern of surface faulting and the location of the well-located aftershocks suggest a possible change of fault strike at a point about 10 km northwest of Highway 46 (Figure 1). To model this break we considered the fault model consisting of two fault planes: one about 20 km long striking N43°W, dipping 85.5°SW; the other about 15 km long striking N31°W, with the same dip angle. Figure 1 shows a horizontal projection of one of the models considered.

The *P*- and *S*-wave velocities in the theoretical infinite homogeneous space problem were chosen to be 5.6 and 3.2 km/sec, respectively. The approximate model with parallel layers for the Cholame Valley area (Eaton *et al.*, 1970) has low-velocity layers to a depth of about 4 km where the *P*-wave velocity increases to 6 km/sec. Although most of the inferred rupture is in the high-velocity layer (Figure 2), the apparent velocity is less than 6 km/sec since all arrivals are delayed by the low-velocity surface layers. To model this effect, we selected the *P*-wave velocity of 5.6 km/sec. To determine the *S*-wave velocity the usual assumption that $\beta = \alpha/\sqrt{3}$ was made.

For all the dislocation models (Table 2) the two fault planes were subdivided into sections 4.4 to 5.2 km long depending on the dislocation velocity. The fault then consisted of seven sections each 6 km wide. For convenience in computer coding, the length of each fault element was chosen to be 2 sec $\times v$ (the rupture velocity). Since the measured displacement data are reduced to equally spaced sequence with $\Delta t = \frac{1}{2}$ sec, it is easier to handle the delays of the origin time for each fault element in terms of the multiples of Δt. In this way the total duration of the source was fixed whereas the total length of faulting increased with the rupture velocity.

Figures 4 through 8 show the comparison of measured and calculated ground displacements at the five strong-motion accelerograph stations of the Cholame-Shandon array. Displacements from the five dislocation models (Table 2) with dislocation velocities

TABLE 2
PARAMETERS DESCRIBING THE DISLOCATION MODELS

Model No.	Dislocation Velocity (km/sec)	φ_1* (deg)	θ_1* (deg)	ψ_1* (deg)	φ_2* (deg)	θ_2* (deg)	ψ_2* (deg)	Δx_1† (km)	Δx_2† (km)	L_1‡ (km)	L_2‡ (km)	N_1§	N_2§	T (sec)
1	2.2	0	47	94.5	0	61	94.5	15.0	−16.0	22.0	8.8	5	2	0.7
2	2.3	0	47	94.5	0	58.5	94.5	12.8	−13.5	18.4	13.8	4	3	0.7
3	2.4	0	47	94.5	0	59	94.5	13.2	−14.1	19.2	14.4	4	3	0.7
4	2.5	0	47	94.5	0	59	94.5	13.5	−14.8	20.0	15.0	4	3	0.7
5	2.6	0	47	94.5	0	61	94.5	14.3	−15.3	20.8	15.6	4	3	0.7

* Referring to Figure 3 the angles φ_i, θ_i and ψ_i ($i = 1, 2$) describe the orientation of the X_1, X_2 and X_3 coordinates in the x_i (east), y_i (north) z_i (up) systems.

† Δx_1 and Δx_2 are the coordinates of the origin of the x_2y_2 coordinate system in the x_1y_1 system (see Figure 1).

‡ L_1 and L_2 are the lengths of northwestern and southeastern fault sections (see Figure 1).

§ N_1 and N_2 are the numbers of fault elements in L_1 and L_2, respectively.

ranging from 2.2 to 2.6 km/sec are shown in all of the figures. The band-pass filtered ground displacements are indicated with 42 dots spaced at 0.5 sec, the only exception being the N25°W component at Station 2 where no strong-motion record was obtained due to instrument malfunction. The rise time T for Haskell's (1969) dislocation function D_1 was chosen to be 0.7 sec for all of the models considered in this paper. This parameter does not appear to influence the computed displacements in a significant way and any value between 0.5 and 1 sec would seem to be acceptable.

Although the acceleration traces recorded during the Parkfield earthquake were of excellent quality, to maximize the reliability of the dislocation model inferred from this data, it was decided to use the records only between 0.11 and 1 Hz. An Ormsby filter with $f_T = 0.10$ Hz and $f_c = 0.12$ Hz (Trifunac, 1971) was used to high-pass filter the calculated displacement curves (Trifunac *et al.*, 1973b) prior to the least-squares-fitting procedure. To allow for a physically meaningful fitting procedure, the calculated displacements from each of the seven fault sections were also high-pass filtered using the same Ormsby filter. The high-frequency cut-off of 1 Hz was realized by a direct decimation process for both the data and the theoretical model. Although the selection of the low-frequency cut-off (0.11 Hz) was governed by the low signal-to-noise ratio for the calculated long-period ground displacements, the high-frequency cut-off (1 Hz) was required by the available computer memory and the adverse effects of scattering and diffraction on seismic waves that are shorter than several kilometers.

The agreement between the calculated and measured horizontal ground displacements (Figures 4 through 8) is good, whereas the agreement for the vertical components is poor to fair. We interpret this as being caused by the low-velocity surface layering which can change significantly the angle-of wave incidence at the recording stations. The effect on the horizontal components of ground motion is expected to be less important for the pure strike-slip faulting assumed in this study.

The agreement between the measured and calculated ground motions, of course, deteriorates with increasing time past the S-wave arrival (see Table 1). This is caused by the surface-wave arrivals which are present in the recorded ground motion but are absent from the calculated displacements. Thus, the above statement that the agreement between the measured and calculated displacements is good refers to the beginning of the strong-motion pulse which is several seconds long and which follows the S-wave arrival

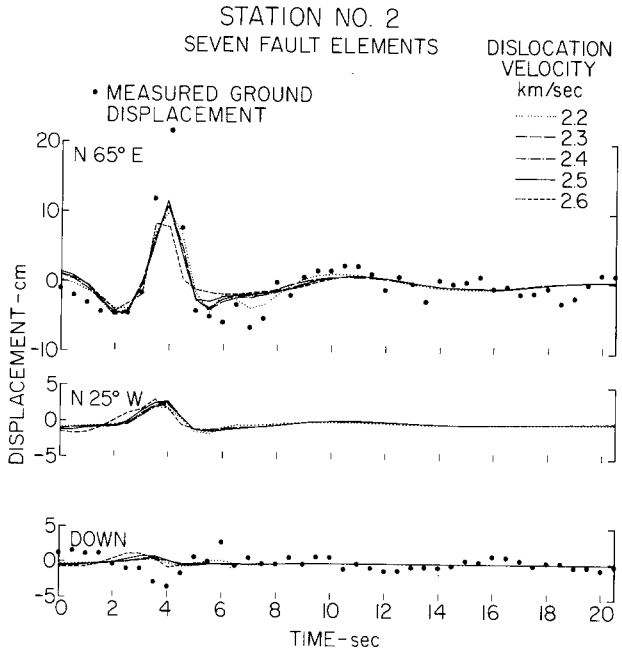
STATION NO. 2
SEVEN FAULT ELEMENTS
DISLOCATION VELOCITY km/sec
2.2
2.3
2.4
2.5
2.6
• MEASURED GROUND DISPLACEMENT
N 65° E
N 25° W
DOWN
DISPLACEMENT - cm
TIME - sec

FIG. 4.

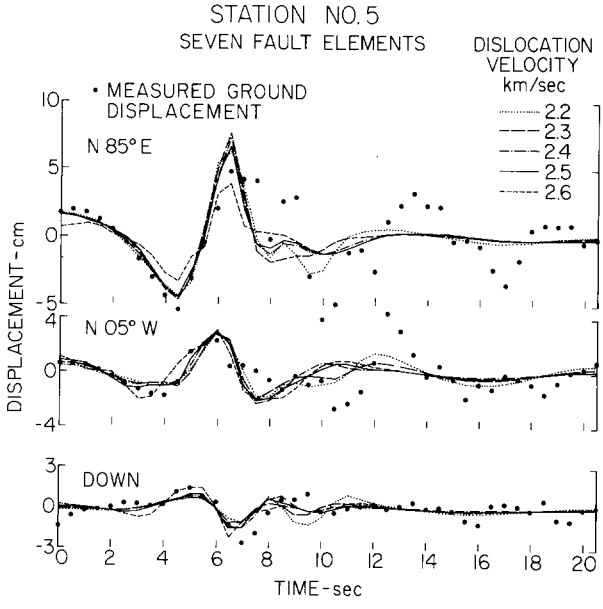
STATION NO. 5
SEVEN FAULT ELEMENTS
DISLOCATION VELOCITY km/sec
2.2
2.3
2.4
2.5
2.6
• MEASURED GROUND DISPLACEMENT
N 85° E
N 05° W
DOWN
DISPLACEMENT - cm
TIME - sec

FIG. 5.

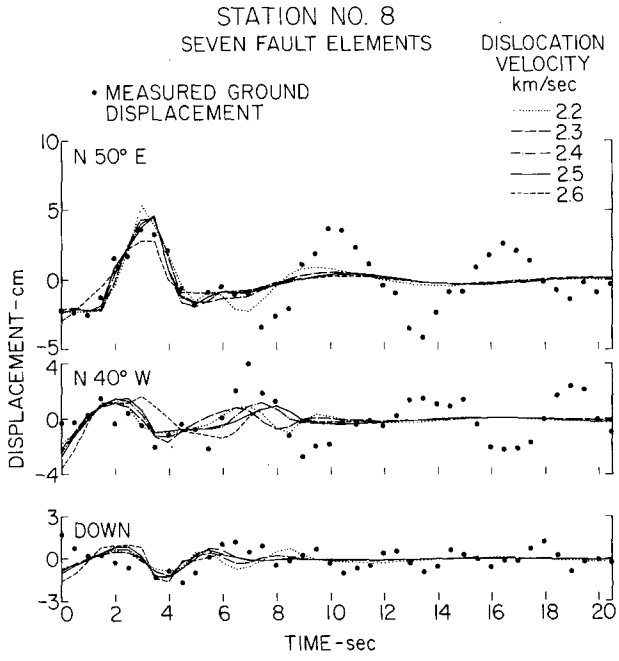
STATION NO. 8
SEVEN FAULT ELEMENTS
DISLOCATION VELOCITY km/sec
2.2
2.3
2.4
2.5
2.6
• MEASURED GROUND DISPLACEMENT
N 50° E
N 40° W
DOWN
DISPLACEMENT-cm
TIME-sec

FIG. 6.

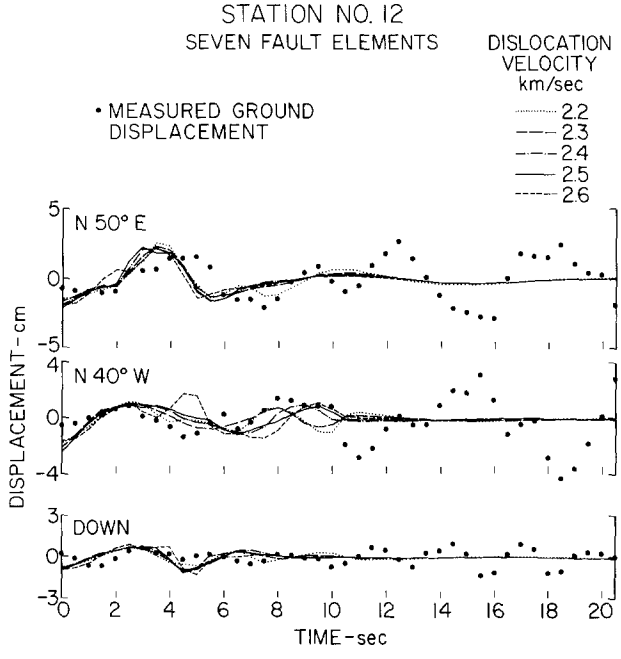
STATION NO. 12
SEVEN FAULT ELEMENTS
DISLOCATION VELOCITY km/sec
2.2
2.3
2.4
2.5
2.6
• MEASURED GROUND DISPLACEMENT
N 50° E
N 40° W
DOWN
DISPLACEMENT-cm
TIME-sec

FIG. 7.

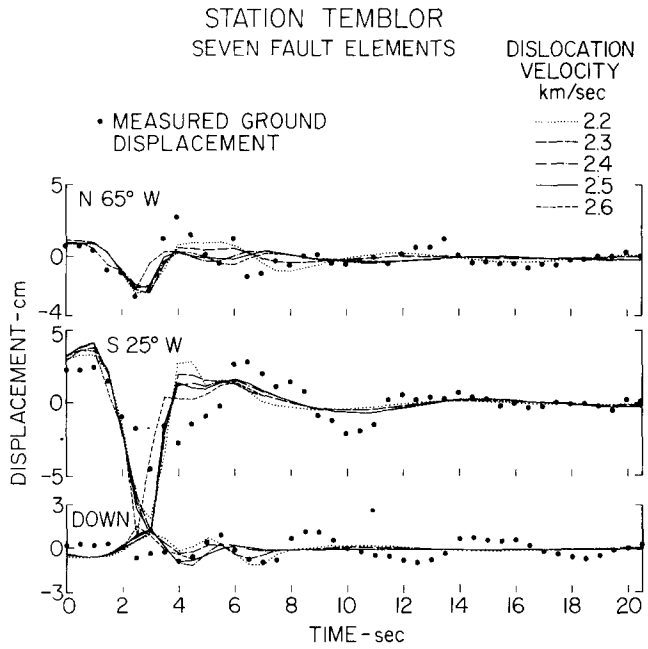

FIG. 8.

time. Rather than fitting only this short displacement record, we prefer to fit the longer section of the recorded ground motion as this minimizes the adverse end effects introduced by the digital filtering. Then, the differences between the calculated and measured ground motions indicate the extent to which the later surface-wave arrivals might contribute to the total ground motion.

The dislocation amplitudes corresponding to the five models in Figures 4 through 8 are shown in Figure 9, a through e, where the seven dislocation amplitudes for the seven elementary faults are plotted versus distance measured from the epicenter in the positive southeast direction along the fault. Three sets of dislocation amplitudes are shown for each dislocation velocity corresponding to $DTSH = -0.1$, -0.2, and -0.3 sec. The S-wave arrival time for the recorded accelerograms has been determined for each station in order to establish a reference time for the S-wave arrival in the theoretical model so that the calculated and measured displacements have a common relative time. Since there is an uncertainty in the choice of this S-wave arrival, a perturbation $DTSH$ of the estimated value is applied simultaneously to all data. Variations of the fitted dislocation amplitudes for various values of $DTSH$ then measure the sensitivity of the inferred models to the errors in reading and interpreting the S-wave arrivals. Additional $DTSH$ shifts equal to 0.0, 0.1, and 0.2 sec are shown for the model with $v = 2.5$ km/sec in Figure 9d. The positive D_i dislocation amplitudes correspond to the right-lateral strike-slip faulting (Figure 3), whereas the negative amplitudes imply the left-lateral strike-slip displacements.

In interpreting the fitted dislocation amplitudes (Figure 9, a through e), a simple but plausible assumption will be made: no reversed faulting is permissible for the final dislocation model. Although a dynamic overshoot and a subsequent locking of the fault cannot be ruled out, in the light of the field observations following the earthquake (Allen and Smith, 1966), it seems very unlikely that the sense of faulting could have been reversed in direction during the main shock. This assumption is supported by creep observations carried out for a year following the earthquake. The summary of these

observations is redrawn from Smith and Wyss (1968) in Figure 9f showing the cumulative right-lateral creep along the entire fault length. Thus, based on this assumption, the models with the dislocation velocity equal to 2.2 and 2.6 km/sec have to be ruled out. Assuming that the variations of several tens of centimeters in dislocation amplitudes result from inaccuracies in the fitting procedures (e.g., poor selection of the *S*-wave arrivals and

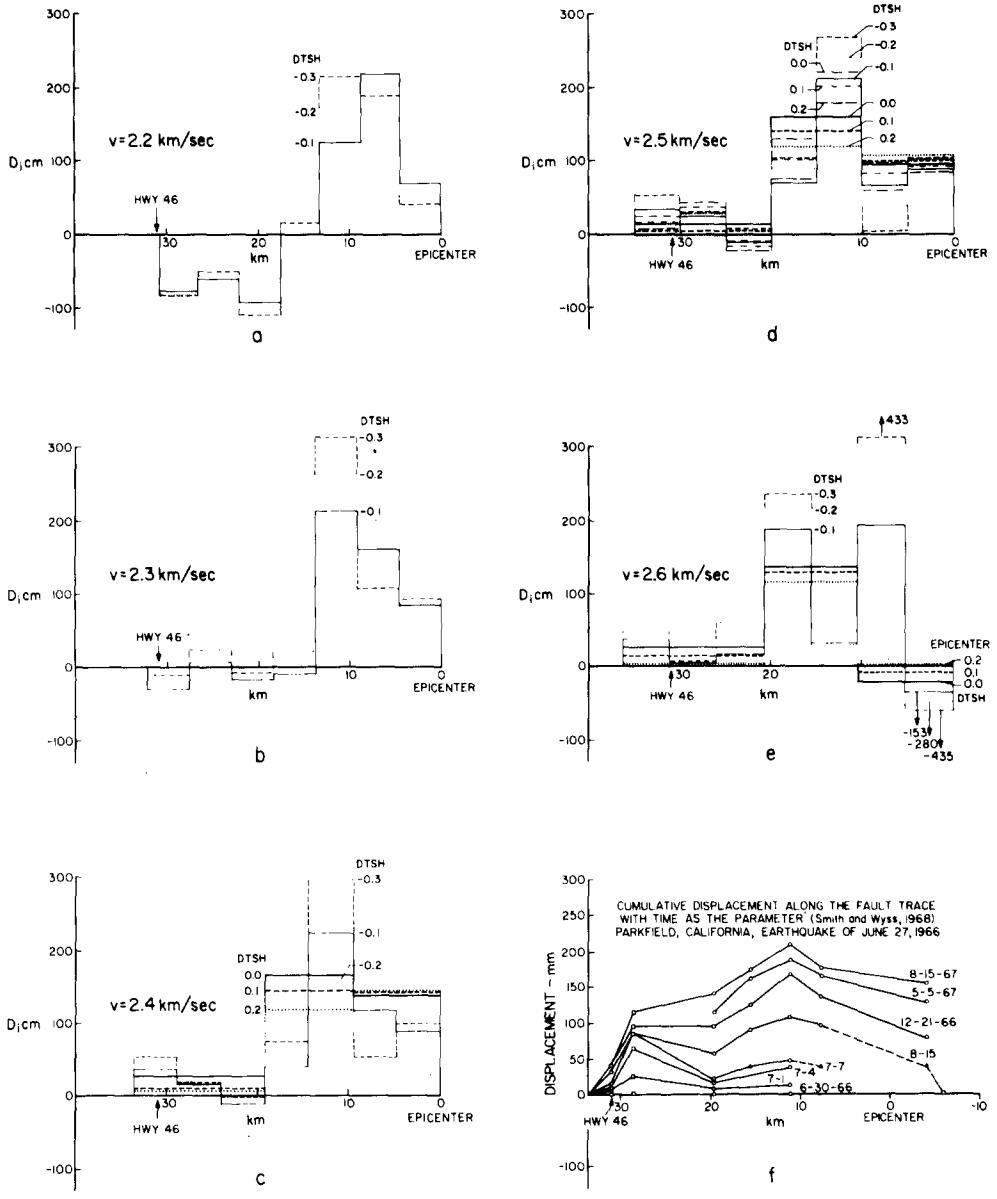

FIG. 9. Computed dislocation amplitudes for five rupture velocities and the observed surface fault offsets.

neglecting the surface-wave contributions), all dislocation models with $v = 2.3$, 2.4, and 2.5 km/sec would be acceptable. The model with $v = 2.3$ km/sec would imply large dislocation amplitudes over a short, about 15 km, fault length and essentially zero amplitudes over the rest of the assumed fault plane. The rupture velocities of 2.4 and 2.5 km/sec would also imply large dislocation amplitudes in the northwestern section

of the fault, about 20 km long, but would lead to small dislocation amplitudes over the southeastern portion of the fault.

The large variations of the dislocation amplitudes (Figure 9, a through e) are not only caused by the oversimplified least-squares-fitting approach, the errors in selecting the *S*-wave arrivals for the recorded accelerograms, and the oversimplified theoretical model, but also by the fact that all of the strong-motion stations were located to the southeast end rather than around the fault. Their location undoubtedly diminished the degree of constraint each accelerogram could have contributed to the fitting procedure.

One might question whether the seven "small" fault elements, 4.4 to 5.2 km long and 6 km wide, indeed depict the significant changes of the dislocation amplitudes along the fault. To examine this point further, the dislocations computed from the first and second, the third and fourth, fifth, sixth, and seventh fault elements were combined before the high-pass filtering. Least-squares-fitting was carried out, this time, for only the three big fault elements. The models with the dislocation velocities of 2.4, 2.5, and 2.6 km/sec were studied in this way. For comparison with previous results, the positive perturbations of the *S*-wave arrivals (Table 1) were now considered with $DTSH = 0.0, 0.1$, and 0.2 sec. The results are shown in Figure 9, c, d and e. The lines corresponding to these values of *DTSH* can be identified by their longer length indicating the longer lengths of fault elements chosen. The apparent effect is that the dislocation amplitudes are smoothed but the trends and the overall amplitudes remain the same. Comparison of measured and calculated displacements is shown in Figures 10 through 14. As can be seen in these figures, the seven fault elements fit the measured displacements better but the main

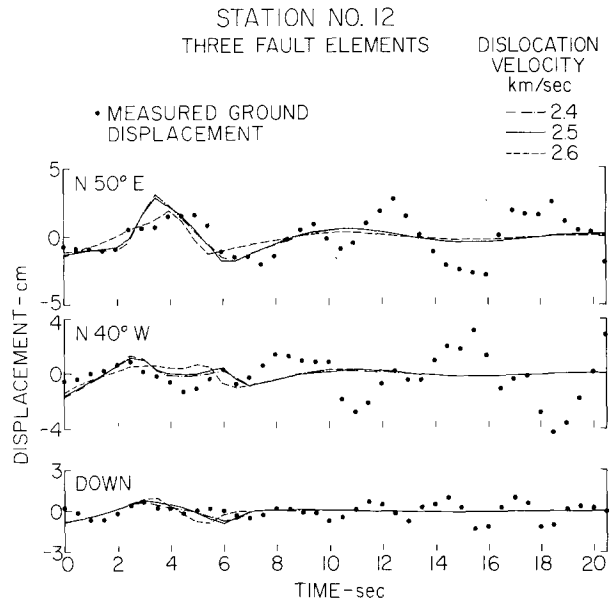

FIG. 10.

trends and the pulse shapes emerging from the fit by the three fault elements are also very good. From Figure 9 and these results, one can conclude that the dislocation velocity during the Parkfield earthquake must have been between 2.3 and 2.5 km/sec while the dislocation amplitudes were about 120 cm along the northwestern section of the fault which was some 20 km long, and less than about 20 cm for the southeastern section which was about 15 km long (Figure 9, a through e). The abrupt decrease of dislocation ampli-

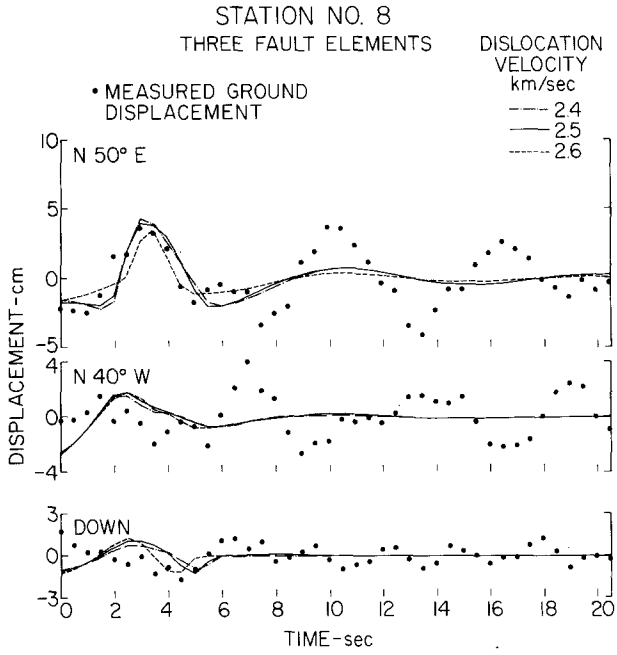

Fig. 11.

tudes some 20 km southeast of the epicenter corresponds closely to the area where Murray (1966) identified seven aftershocks that were recorded during the first several minutes immediately following the main shock.

Based on the strong-motion data above, it seems then, that the significant faulting must have stopped about 20 km southeast of the epicenter rather than in the vicinity of Highway 46. Whether the southeastern section of the fault did indeed fracture by a small amount during the main shock or gave way later during some of the subsequent aftershocks and creep is a difficult question to answer with certainty, inasmuch as the later

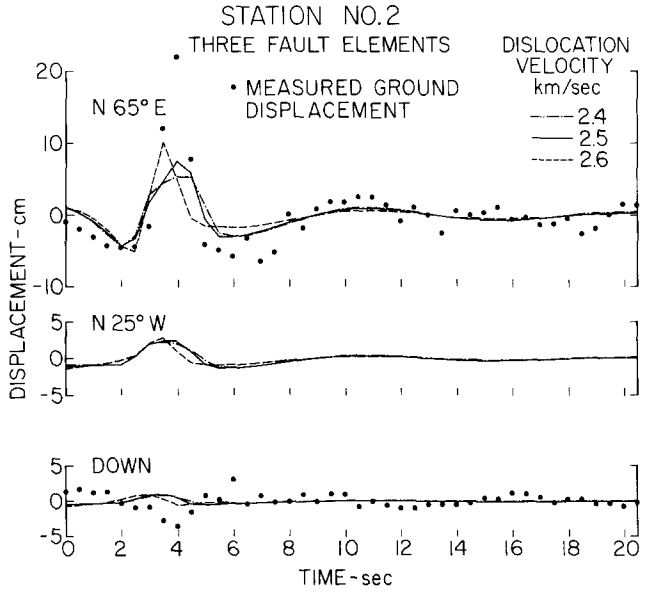

Fig. 12.

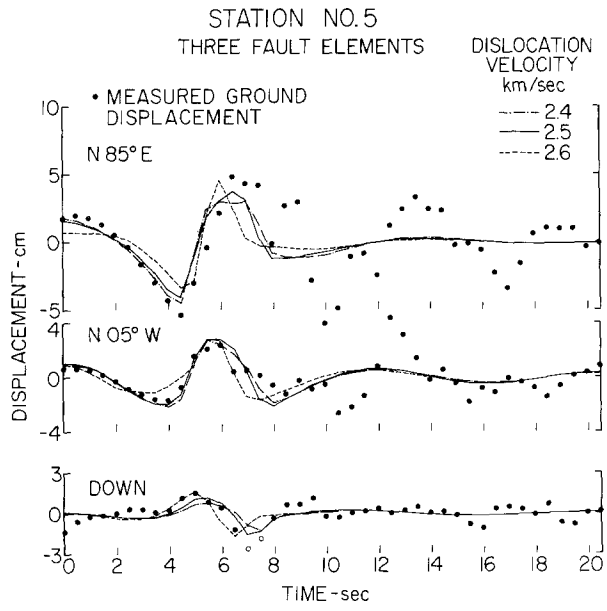

FIG. 13.

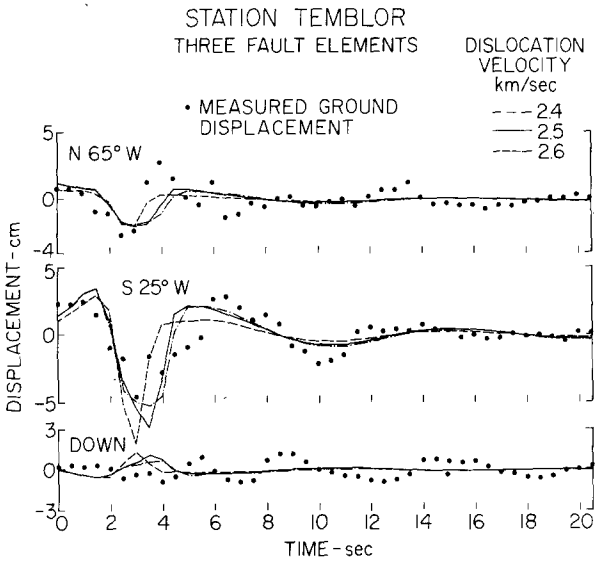

FIG. 14.

portion of the strong ground motions from which this information has to be derived may be seriously affected by the surface waves. Yet, it is interesting that this interpretation supports the suggestions made by Lindh and Boore (1973) that only small displacements occurred in the southeastern section of the fault.

A point-by-point comparison of calculated and recorded strong-motion pulses in Figures 4 through 8 and 10 through 14, for the time interval immediately following the *S*-waves, shows that in several cases peak amplitudes disagree by as much as a factor of two (e.g. N65°E component at Station 2 and S25°W component at Station Temblor). We do not consider this to be a significant discrepancy since all of the data in this approximate analysis have been fitted simultaneously and because the sizes of the elementary fault elements employed in the analysis are too large to bring out all of the fine details.

Figure 9f summarizes the creep measurements of Smith and Wyss (1968) in an attempt to compare their results with the inferred dislocation amplitudes. As seen in this figure, until July 7 the cumulative displacement across the fault had the highest rate of displacement increase at about 5 km northwest of Highway 46. In subsequent months, the main creep activity migrated to the northwestern section of the fault.

Our model is based on the assumption of Scholz *et al.* (1969) that the main shock did not propagate to the surface. Because this would lead to high-stress concentrations between the slipped region and the surface and consequently to creep, the nature of the observed fault displacements in the months following the earthquake (Smith and Wyss, 1968) represents a strong support to the buried fault assumption. The long-term distribution of the relative surface displacements along the fault, resulting from such creep, might then be expected to reflect the distribution of dislocation amplitudes at depth. In other words, although the surface offsets would most probably display amplitudes which are significantly smaller than those at depth, we expect that there should be a strong similarity between the two displacement patterns at the surface and at depth. From this viewpoint the agreement between the computed dislocation amplitudes in Figure 9, c and d, and the cumulative displacement plot shown in Figure 9f is very good. Although the observed creep along the 10-km-long southeasternmost section of the fault could have resulted from later aftershocks spreading away from the dislocation end, it is also possible that the observed cumulative creep shown in Figure 9f could be the direct result of the strike slip motions at depth generated by the main shock. If we were to assume the latter, then the two models with the dislocation velocities equal to 2.4 and 2.5 km/sec would become the best candidates for the final model.

Large cumulative displacements in Figure 9f suggest the possibility of bilateral faulting, i.e., an additional fault propagating toward northwest and away from the instrumentally determined epicenter. To explore this possibility further, we added one fault element, 4.8 km long and 6 km wide, to the model no. 3 (Table 2). The orientation of this fault can be given by $\varphi_3 = 0$, $\theta_3 = 227°$, and $\psi = 85.5°$. The dislocation velocity of 2.4 km/sec toward the northwest was assumed. The fitted dislocation amplitudes were found to have an alternating direction, indicating a very poor fit to the data. Although one unsuccessful trial is, of course, not sufficient to reject the possibility of bilateral faulting during the Parkfield earthquake, we decided to accept a unilateral source model as a simple approximate model. This decision is supported by Anderson's (1973) work which shows that the bilateral fault model does not change significantly the calculated displacements at distances of about 30 to 35 km to the southeast.

Comparison of the Dynamic Model with Geodetic Data and Previous Estimates of Seismic Moment

The dislocation amplitudes inferred from the strong-motion accelerograms reflect at best the extent of faulting during the several tens of seconds of the main shock. Geodetic measurements, on the other hand, are carried out over long time intervals, usually several years long, and thus may reflect contributions from other earthquakes, preshocks, aftershocks, and creep. For this reason, the dislocation amplitudes inferred from the geodetic data represent an upper bound for the same amplitudes determined by some dynamic measuring process.

In October 1965, the Department of Water Resources of California established geodimeter lines in the Cholame Valley area in the form of a pentagon (Figure 1) consisting of the stations: Kenger (no. 1), Bonnie (no. 2), Mason (no. 3), Cottonwood (no. 4) and Bench (no. 5) (Morrison *et al.*, 1966). Following the Parkfield earthquake, the

Department of Water Resources (1968a, b) remeasured this network in July, 1966. The movement vectors were derived by assuming that the line 3–5 (Mason to Bench) remained fixed. The results indicated that points 6 to 8 km distant from the fault moved about 20 cm in the right-lateral direction relative to the line 3–5 (Figure 1).

A comparison of the pre- and post-earthquake geodetic surveys yields only the relative displacements of the stations, although any rigid body motion may be applied to the net as a whole without changing the relative displacements. Thus, to infer the static dislocation amplitudes on the fault, relative displacements between the geodetic stations have to be considered and compared with the measurements. In this calculation, we have neglected the possible important effects of the shallow surface deposits while assuming that we are dealing with an homogeneous elastic medium.

Figures 15 and 16 summarize the results for the static dislocation model whose geometry has been chosen to be that of the dynamic model no. 4 (Table 2). Figure 15 shows the static displacement field at all five pentagon stations for the four different distributions of dislocation amplitudes: (1) uniform dislocation over the entire fault length, (2) uniform dislocation over the northwestern section of the fault only, (3) variable dislocation amplitudes corresponding to the dynamic dislocation model consisting of three fault elements with rupture velocity of 2.5 km/sec and for $DTSH = 0.1$ (Figure 9d), and (4) variable dislocation amplitudes for the dynamic model consisting of seven fault elements ($DTSH = -0.3$ in Figure 9d) and for the dislocation velocity of 2.5 km/sec. From these displacements, relative distance changes between all possible pairs of stations can be calculated and compared with observations. This comparison is summarized in Figure 16.

The measured distance changes in the pentagon were reported on three different occasions and the numerical results presented differed slightly depending on the mode of

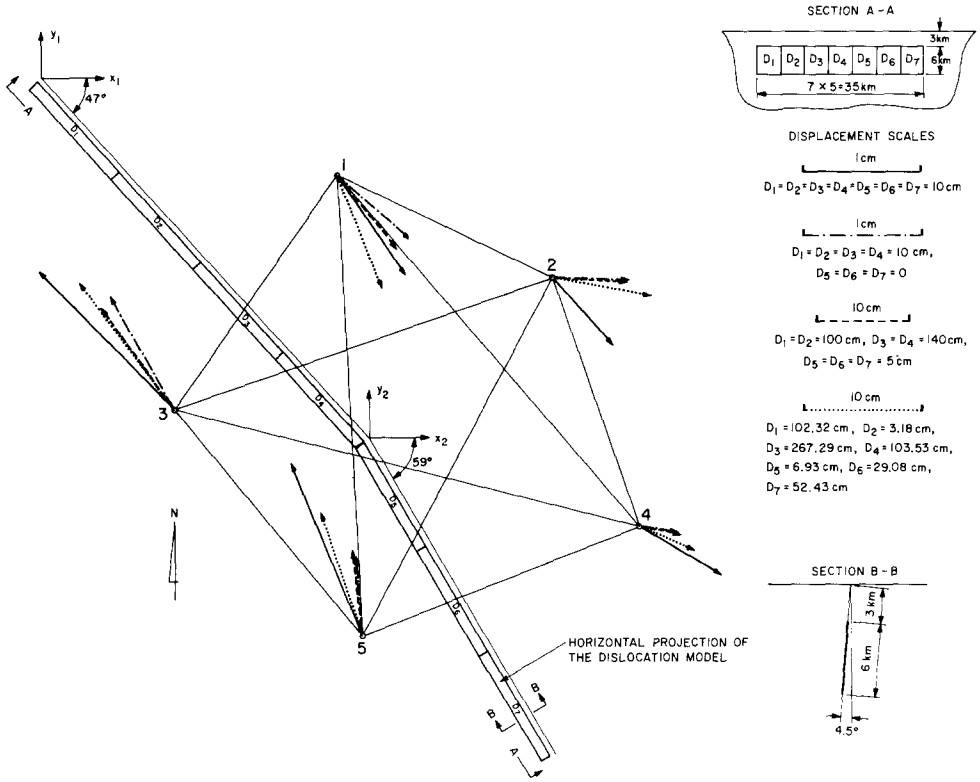

FIG. 15. Computed horizontal displacements—Parkfield, California, earthquake of June 27, 1966.

data presentation. Because the differences between the raw data and the adjusted data probably illustrate the degree of uncertainty inherent in geodetic measurements (R. B. Hofmann, personal communication), measured distance changes are shown in Figure 16 with bars connecting the smallest and the largest estimate in the group. The data for these bars were taken from the two bulletins of the Department of Water Resources (1968a, b) and from the paper by Morrison *et al.* (1966). The accuracy of the above geodetic

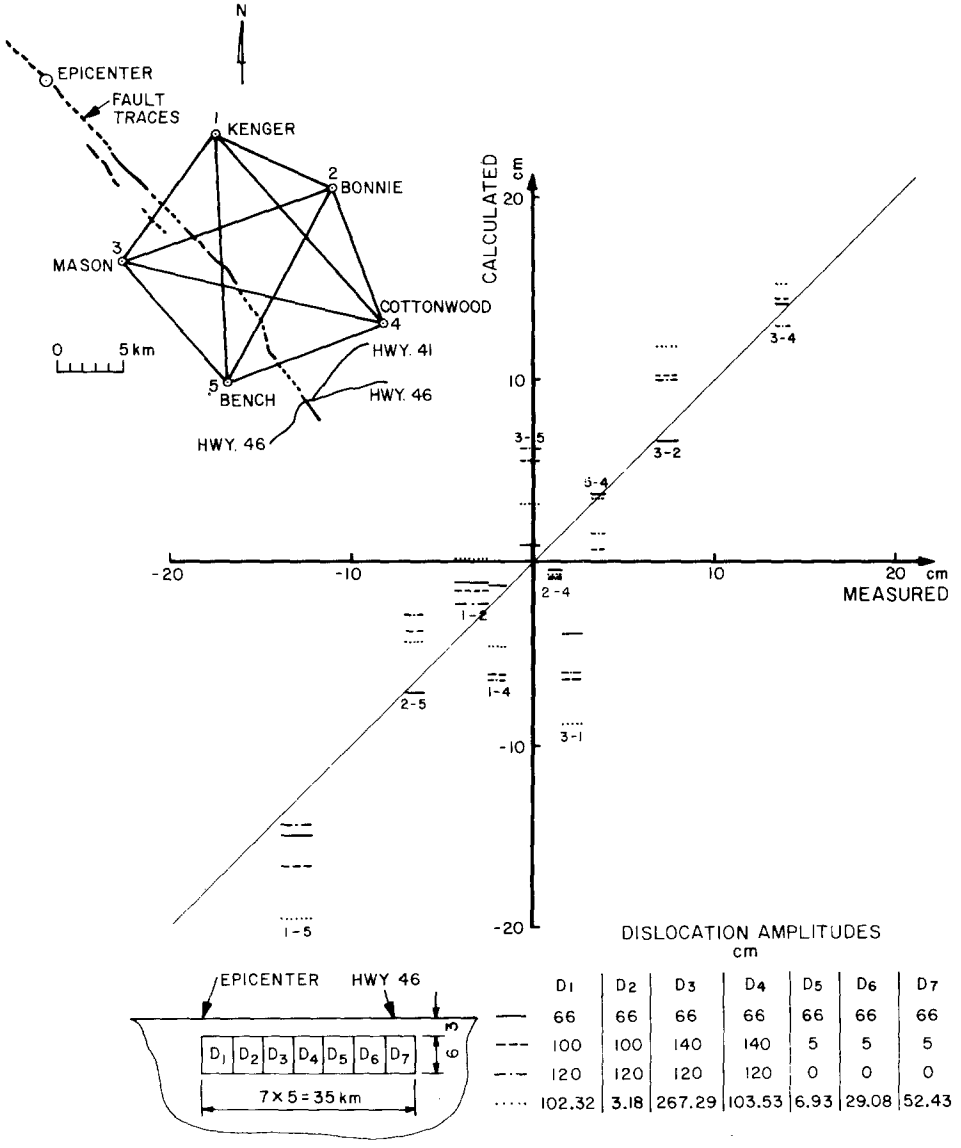

FIG. 16. Comparison of measured and calculated distance changes following the Parkfield, California, earthquake of June 27, 1966.

measurements is at best equal to about 1 part in 10^6 (R. B. Hofmann, personal communication) which means that the distance changes measured for two points some 10 km apart (say Kenger to Bonnie) would be good to within ± 1 cm, whereas the accuracy for the longest line Mason to Cottonwood (Figure 16) would be only within about ± 2 cm. These error estimates are of the same order as the spread of the three reported sets of measured data.

In an ideal case, the measured and calculated distance changes between the different pairs of pentagon points would be identical and all bars in Figure 16 would fall on the 45° line. For the uniform dislocation model with the assumed amplitudes equal to 10 cm and for the model with uniform amplitudes over the northwestern section of the fault only, it is, of course, necessary to find the proper scaling factors so that the measured and calculated data cluster around the 45° line. With these factors equal to 6.6 and 12, respectively, all amplitudes for the four models analyzed are as shown in the table of Figure 16. Considering the approximate nature of the analysis and the uncertainty of the assumptions made, the agreement between the measured and the calculated distance changes is very good. In particular for lines 1–5, 2–5, 3–2, and 3–4, which are the most sensitive to strike-slip motion, the agreement is indeed very good.

In the simplest case, the agreement between the measured and calculated distance changes in Figure 16 would be such that only one dislocation model could be said to fit the data well. Although in this analysis the uniform model with $D = 66$ cm seems to be perhaps the best in this respect, the small differences in final results indicate that all four models fit the data quite well. On a relative basis, however, the best fit is obtained from the uniform model and for the two models with essentially all faulting along the northwestern section of the fault ($D_1 = D_2 = 100$ cm; $D_3 = D_4 = 140$ cm; $D_5 = D_6 = D_7 = 5$ cm and $D_1 = D_2 = D_3 = D_4 = 120$ cm; $D_5 = D_6 = D_7 = 0$ cm.)

As already pointed out in comparing the static and the dynamic inferences about the dislocation amplitudes, we would expect the results of the static analysis to yield larger average dislocation amplitudes. This would be caused by the aftershock activity and creep following the earthquake, factors which cannot usually be eliminated from the geodetic data because of the time involved in these measurements. The strong-motion measurements on the other hand are available for the time during the main shock only and thus contain information on the dislocation amplitudes corresponding to the main energy release only. Comparing the results in Figure 9, c and d, with those in Figure 16, we find that the static and dynamic analyses lead to essentially the same dislocation amplitudes. This could mean that during the 2 weeks immediately following the earthquake, the creep and aftershock activity contributed insignificant amounts to the displacement of the pentagon points. The contributions to the static displacement field resulting from the subsequent creep in the shallow highly strained region above the dynamic dislocation surface must have been confined to a narrow zone (perhaps 5 to 10 km wide) around the fault (Scholz *et al.*, 1969). If this interpretation is correct, then it is possible that the additional motions of the pentagon points in the months following the main shock were only minor.

For the static and dynamic models with $D_1 = D_2 = 100$ cm, $D_3 = D_4 = 140$ cm and $D_5 = D_6 = D_7 = 5$ cm and the rigidity of 3×10^{11} dyne/cm^2, we obtain the seismic moment equal to 4.4×10^{25} dyne-cm. This value is about three times larger than 1.4×10^{25}, the value quoted by Aki (1968) and determined by him from the spectra of long-period surface waves observed at long distances. It is about two times larger than the moment of 1.9×10^{25} dyne-cm used by Scholz *et al.* (1969). Since in general the moment determination from the spectra of distant seismic waves is good to within a factor of 2–3, our moment does not contradict the previous estimates seriously. Inaccuracies of similar extent (factor of 2–3) may therefore occur in the determination of the average dislocation amplitudes from such estimates of the seismic moment.

CONCLUSIONS

This study represents another example of source mechanism analysis based on strong-

motion accelerograph records. It is based on numerous simplifying assumptions and procedures which range from an elementary plane dislocation in an infinite elastic and homogeneous space, which does not support surface waves, to the use of band-pass filtered ground acceleration in the frequency band between about 0.1 and 1 Hz. In spite of these simplifications, quite detailed and valuable information on the earthquake faulting process could be obtained.

It has been found that observations and measurements of the Parkfield earthquake can be explained in terms of a buried fault some 20 km long extending from a depth of 3 to 9 km with a dislocation amplitude of about 120 cm which propagated from the epicenter toward the southeast. This model is consistent with all of the strong-motion data, with the geodetic measurements an the cumulative creep readings following the earthquake.

It seems that the time and space behavior at an earthquake dislocation may be determined in the frequency band lower than about 1 Hz by using the strong-motion accelerograph recordings in the immediate near-field of an earthquake source. Although this task involves the solution of an inverse problem which has no unique solution, combining the geodetic and teleseismic data with the measurements of the strong ground motion appears to provide sufficient constraints for a detailed dislocation model to be determined.

Acknowledgments

We are indebted to G. W. Housner and D. E. Hudson of the California Institute of Technology and to J. Anderson of the Lamont-Doherty Geological Observatory of Columbia University for critical reading of the manuscript.

This research was supported by the Advanced Research Project Agency of the Department of Defense and was monitored by the Air Force Office of Scientific Research under Contract F44620-72-C-0097.

References

Allen, C. R. and S. W. Smith (1966). Parkfield earthquake of June 27–29, 1966, pre-earthquake and post-earthquake surficial displacement, *Bull. Seism. Soc. Am.* **56,** 955–967.

Aki, F. (1968). Seismic displacements near a fault, *J. Geophys. Res.* **73,** 5359–5376.

Anderson, T. (1973). A model source-time function for the Parkfield, California, earthquake, (*Abstract*) 68th Annual National Meeting of the Seismological Society of America, Golden, Colorado.

Birch, F. (1961). The velocity of compressional waves in rocks to 10 kilobars, 2, *J. Geophys. Res.* **66,** 2199–2224.

Brown, R. D. Jr. and J. G. Vedder (1966). Surface tectonic fractures along the San Andreas Fault, The Parkfield-Cholame California earthquakes of June–August 1966, *U.S. Geol. Surv. Profess. Paper 579.*

Cloud, W. K. (1967). Intensity map structural damage, Parkfield, California, earthquake of June 27, 1966, *Bull. Seism. Soc. Am.* **57,** 1161–1178.

Cloud, W. K. and V. Perez (1967). Accelerograms—Parkfield earthquake, *Bull. Seism. Soc. Am.* **57,** 1179–1192.

Department of Water Resources of California (1968a). Earthquake Engineering Programs, *Bulletin No. 116–4*, p. 75.

Department of Water Resources of California (1968b). Geodimeter Fault Movement Investigations in California, *Bulletin No. 116–6*, p. 49.

Eaton, J. P. (1967). The Parkfield-Cholame, California, earthquakes of June–August 1966; instrumental seismic studies, *U.S. Geol. Surv. Prof. Paper 579.*

Eaton, J. P., M. E. O'Neill and J. N. Murdock (1970). Aftershocks of the 1966 Parkfield-Cholame, California, earthquake: A detailed study, *Bull. Seism. Soc. Am.* **60,** 1151–1197.

Filson, J. and T. V. McEvilly (1967). Love-wave spectra and the mechanism of the 1966 Parkfield sequence, *Bull. Seism. Soc. Am.* **57,** 1245–1257.

Haskell, N. A. (1969). Elastic displacements in the near-field of a propagating fault, *Bull. Seism. Soc. Am.* **59,** 865–908.

Housner, G. W. and M. D. Trifunac (1967). Analysis of accelerograms—Parkfield earthquake, *Bull. Seism. Soc. Am.* **57,** 1193–1220.

Hudson, D. E. and W. K. Cloud (1967). Analysis of seismoscope data from Parkfield earthquake of June 27, 1966, *Bull. Seism. Soc. Am.* **57,** 1143–1159.

Kasahara, K. A. (1964). A strike-slip fault buried in a layered medium, *Bull. Earthquake Res. Inst., Tokyo Univ.* **42,** 609–620.

Lindh, A. G. and D. M. Boore (1973). Another look at the Parkfield earthquake using strong-motion instruments as a seismic array. (*Abstract*) 68th Annual National Meeting of the Seismological Society of America, Golden, Colorado.

McEvilly, T. V. (1966). Preliminary seismic data, June–July, 1966 in Parkfield earthquakes of June 27–29, 1966, Monterey and San Luis Obispo Counties, California—preliminary report, *Bull. Seism. Soc. Am.* **56,** 967–971.

McEvilly, T. V., W. H. Bakum and K. B. Casaday (1967). The Parkfield, California, earthquakes of 1966, *Bull. Seism. Soc. Am.* **57,** 1221–1244.

Meade, B. K. (1967). Report on results of triangulation for earth movement study, vicinity of Cholame, California, U.S. Coast and Geodetic Survey, Washington Science Center.

Morrison, P. W., R. B. Hofmann, and J. E. Wolfe (1966). Parkfield earthquakes, June 28–29, 1966, *Earthquake Notes* **37,** 5–18.

Murray, G. F. (1967). Note on strong motion records from the June 1966 Parkfield, California, earthquake sequence, *Bull. Seism. Soc. Am.* **57,** 1259–1266.

Scholz, C. H., M. Wyss and S. W. Smith (1969). Seismic and aseismic slip on the San Andreas Fault, *J. Geophys Res.* **74,** 2049–2069.

Smith, S. W. and M. Wyss (1968). Displacement on the San Andreas Fault subsequent to the 1966 Parkfield earthquake, *Bull. Seism. Soc. Am.* **58,** 1955–1973.

Tsai, Y. B. and H. J. Patton (1973). Interpretation of the strong-motion earthquake accelerograms using a moving dislocation model: The Parkfield, California, earthquake of June 28, 1966. (*Abstract*) 68th Annual National Meeting of the Seismological Society of America, Golden, Colorado.

Trifunac, M. D. (1971). Zero base-line correction of strong motion accelerograms, *Bull. Seism. Soc. Am.* **61,** 1201–1211.

Trifunac, M. D. (1972). A note on correction of strong-motion accelerograms for instrument response, *Bull. Seism. Soc. Am.* **62,** 401–409.

Trifunac, M. D., F. E. Udwadia and A. G. Brady (1973a). Analysis of errors in digitized strong-motion accelerograms, *Bull. Seism. Soc. Am.* **63,** 157–187.

Trifunac, M. D., A. G. Brady and D. E. Hudson (1973b). Strong motion earthquake accelerograms, Vol. II, Part B, corrected accelerograms and integrated ground velocity and displacement curves, *Report No. EERL 73–55*, Earthquake Engineering Research Laboratory, California Institute of Technology, Pasadena.

Trifunac, M. D. (1974). A three-dimensional dislocation model for the San Fernando, California, earthquake of February 9, 1971, *Bull. Seism. Soc. Am.* **64,** 149–172.

Wallace, R. E. and E. F. Roth (1967). The Parkfield-Cholame, California earthquakes of June-August, 1966—rates and patterns of progressive deformation, *U.S. Geol. Surv. Profess. Paper, 579,* 23–39.

EARTHQUAKE ENGINEERING RESEARCH LABORATORY
CALIFORNIA INSTITUTE OF TECHNOLOGY
PASADENA, CALIFORNIA 91109

Manuscript received October 27, 1973.